JGR Space Physics

RESEARCH ARTICLE
10.1029/2019JA027654

Extreme Magnetosphere-Ionosphere-Thermosphere Responses to the 5 April 2010 Supersubstorm

Y. Nishimura[1], L. R. Lyons[2], C. Gabrielse[3], N. Sivadas[1], E. F. Donovan[4], R. H. Varney[5], V. Angelopoulos[6], J. M. Weygand[6], M. G. Conde[7], and S. R. Zhang[8]

[1]Department of Electrical and Computer Engineering and Center for Space Physics, Boston University, Boston, MA, USA, [2]Department of Atmospheric and Oceanic Sciences, University of California, Los Angeles, CA, USA, [3]The Aerospace Corporation, Los Angeles, CA, USA, [4]Department of Physics and Astronomy, University of Calgary, Calgary, Alberta, Canada, [5]SRI International, Menlo Park, CA, USA, [6]Department of Earth, Planetary and Space Sciences, University of California, Los Angeles, CA, USA, [7]Department of Physics, University of Alaska Fairbanks, Fairbanks, AK, USA, [8]MIT Haystack Observatory, Westford, MA, USA

Key Points:
- The supersubstorm is characterized by unusually large expansion-phase auroral brightenings, including a PBI and auroral streamer
- The supersubstorm also had an intense SCW, plasma flow, particle injection and precipitation, TEC, conductance and wind
- Extreme responses were caused by unusually large energy accumulation and release by localized tail reconnection and particle acceleration

Supporting Information:
- Supporting Information S1
- Movie S1

Correspondence to:
Y. Nishimura,
toshi16@bu.edu

Citation:
Nishimura, Y., Lyons, L. R., Gabrielse, C., Sivadas, N., Donovan, E. F., Varney, R. H., et al. (2020). Extreme magnetosphere-ionosphere-thermosphere responses to the 5 April 2010 supersubstorm. *Journal of Geophysical Research: Space Physics*, *125*, e2019JA027654. https://doi.org/10.1029/2019JA027654

Received 19 NOV 2019
Accepted 27 MAR 2020
Accepted article online 4 APR 2020

Abstract The extreme substorm event on 5 April 2010 (*THEMIS AL* = −2,700 nT, called supersubstorm) was investigated to examine its driving processes, the aurora current system responsible for the supersubstorm, and the magnetosphere-ionosphere-thermosphere (M-I-T) responses. An interplanetary shock created shock aurora, but the shock was not a direct driver of the supersubstorm onset. Instead, the shock with a large southward IMF strengthened the growth phase with substantially larger ionosphere currents, more rapid equatorward motion of the auroral oval, larger ionosphere conductance, and more elevated magnetotail pressure than those for the growth phase of classical substorms. The auroral brightening at the supersubstorm onset was small, but the expansion phase had multistep enhancements of unusually large auroral brightenings and electrojets. The largest activity was an extremely large poleward boundary intensification (PBI) and subsequent auroral streamer, which started ~20 min after the substorm auroral onset during a steady southward IMF B_z and elevated dynamic pressure. Those were associated with a substorm current wedge (SCW), plasma sheet flow, relativistic particle injection and precipitation down to the D-region, total electron content (TEC), conductance, and neutral wind in the thermosphere, all of which were unusually large compared to classical substorms. The SCW did not extend over the entire nightside auroral activity but was localized azimuthally to a few 100 km in the ionosphere around the PBI and streamer. These results reveal the importance of localized magnetotail reconnection for releasing large energy accumulation that can affect geosynchronous satellites and produce the extreme M-I-T responses.

Plain Language Summary Supersubstorms are extreme space weather events that involve unusually intense aurora. The goal of this study is to understand the driving processes and system responses during a supersubstorm event on 5 April 2010, when the Intelsat Galaxy-15 experienced an anomaly and stopped responding to ground commands. We found that the supersubstorm was associated with a particular type of aurora called poleward boundary intensification and a subsequent auroral streamer. This type of aurora can often occur, but the one in this event was unusually large (*AL* = −2,700 nT), in association with extremely intense currents and relativistic particle acceleration. The accelerated particles precipitated down to 60 km altitude, much lower than the typical height of aurora (>100 km). This event was caused by extremely intense magnetic reconnection and fast flows toward the Earth. This event also created a fast stream of neutral species in the upper atmosphere.

1. Introduction

Particle injection, precipitation, and related electric fields and currents during substorms are a major energy source for the radiation belts and ring current in the magnetosphere and energy dissipation in the ionosphere and thermosphere. Extreme substorm events, called supersubstorms (*AL* < −2,500 nT) (Tsurutani et al., 2015), can even give rise to space weather effects such as satellite anomalies, radio signal scintillations, and ground induced currents. While space weather effects are often perceived as results of major storms and solar flares, a substantial portion of space weather events is actually tied to substorms due to intense

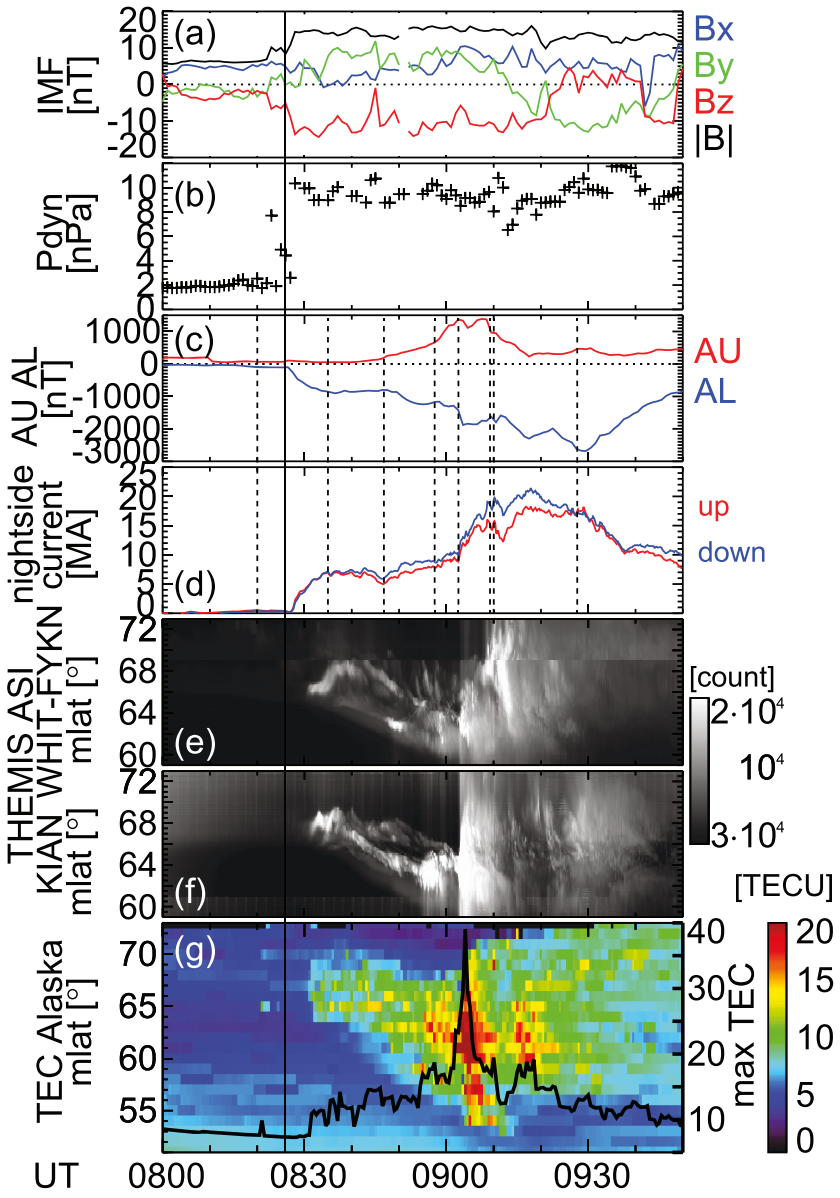

Figure 1. Geotail measurements of the (a) IMF and (b) dynamic pressure, (c) THEMIS *AU* and *AL*, (d) integrated upward and downward currents from the SECS method over North America, THEMIS ASI keogram at (e) White Horse (WHIT) and Fort Yukon (FYKN), (f) Kiana (KIAN), and (g) GPS TEC keogram over Alaska and maximum TEC. The solid vertical line marks the time of the dynamic pressure jump. The dashed lines correspond to times of snapshots in Figure 2.

injection, precipitation, and ionosphere currents (Koons & Fennell, 2006; Tsurutani et al., 2015). Supersubstorms are much less frequent (~2 events per year) than classical substorms (a few events per day) (Hajra et al., 2016). However, once it occurs, the energy release during supersubstorms is so large that the magnetosphere-ionosphere-thermosphere (M-I-T) system can be severely affected.

The 5 April 2010 supersubstorm event, which occurred despite it being a solar minimum, has received strong attention due to its extreme *AL* magnitude and space weather effects. This event (*THEMIS AL* = −2,700 nT, Figure 1c) created an unusual level of energetic electron fluxes associated with an overdipolarization at nightside geosynchronous orbit, which have been assessed as a likely cause of the Galaxy-15 satellite anomaly through electrostatic discharge (Clilverd et al., 2012; Connors et al., 2011; Loto'aniu et al., 2015). Satellite and auroral observations showed that the dominant magnetotail response to the interplanetary shock that

preceded the supersubstorm was fast flow channels and associated auroral streamers (Yue et al., 2013). Global Navigation Satellite System (GNSS) receivers at nightside high latitudes during this event detected large phase scintillation (>1 radian) with numerous cycle slips (Kinrade et al., 2012; Prikryl et al., 2011). In addition, there is ample community interest in this type of extreme event, and this event has received a particular attention for investigating extreme responses, including field-aligned currents (FACs) (Anderson et al., 2017), ring current (Buzulukova et al., 2013; Keesee et al., 2014), and the ionosphere-thermosphere system (Cander, 2016; Lu et al., 2014; Victor et al., 2016).

To no surprise, supersubstorms are associated with a southward interplanetary magnetic field (IMF) during interplanetary magnetic clouds or sheaths (Hajra et al., 2016; Tsurutani et al., 2015). However, the level of the southward IMF (−10 to −20 nT) is not unusual; rather, it is often seen during intense substorms ($AL \sim -1{,}000$ nT) and storms ($Dst < \sim -100$ nT). Interestingly, while supersubstorms do occur during intense storms, they also occur during non-storm intervals (Hajra et al., 2016). The 5 April 2010 event was during a non-storm interval ($Dst \sim -20$ nT). It has been suggested that some supersubstorms are triggered by solar wind dynamic pressure pulses (Tsurutani et al., 2015), but as shown below, the 5 April 2010 event was not directly triggerred by the interplanetary shock.

In the present study, we address (1) what are solar wind driving conditions of supersubstorms and what are the M-I-T system conditions prior to auroral onset of the supersubstorm, (2) what type of aurora and current system is responsible the supersubstorm, and (3) what are M-I-T responses to the supersubstorm. Answers to these questions will advance our understanding of fundamental Geospace system responses to extreme driving conditions. Supersubstorms are rare events that release extreme amounts of energy in the magnetosphere, posing a unique challenge for understanding the unusual levels of M-I-T system responses to extreme driving and space weather phenomena. Thanks to the unprecedented suite of both space-based and ground-based instrumentation, we now have the instruments required to evaluate and understand the fundamental properties of supersubstorms.

2. Results

2.1. Solar Wind and Aurora

Figures 1a and 1b show solar wind parameters measured by Geotail. Geotail was located just upstream of the bow shock ($X_{GSM} = 14$ and $Y_{GSM} = -3$ R_E) and provided accurate solar wind conditions that have driven the 5 April 2010 event. Figures 1c1g show the Time History of Events and Macroscale Interactions during Substorms (THEMIS) *AU* (red) and *AL* (blue) indices, upward and downward currents using the spherical elementary currents systems (SECS) method and the network of ground magnetometers (Weygand et al., 2011), pre-midnight auroral keograms from selected THEMIS ASI stations, and global positioning system (GPS) total electron content (TEC) in Alaska (Vierinen et al., 2016). The upward and downward currents were integrated over North America within ±3 hr from midnight and above 50° MLAT. Selected snapshots of the THEMIS ASI data in Figure 2 give a 2-D sequence of aurora. The whole sequence is shown in Movie S1.

Before 08:26 UT, |*AL*| and upward/downward currents were small (Figures 1c and 1d) and aurora was weak (Figure 2a) under a small southward IMF (~ − 3 nT). Then, an interplanetary shock arrived with a large southward IMF (Figures 1a and 1b). The southward IMF lasted until ~09:25 UT, and the elevated dynamic pressure continued beyond the time interval of interest until 12:30 UT, when a magnetic cloud arrived at 1 AU. During this entire time interval after the shock, Geotail was in the sheath ahead of the magnetic cloud (Liu et al., 2011). |*AL*| increased to ~900 nT, and the upward and downward currents increased to 7 MA. The aurora showed a small brightening and poleward motion (Figures 1e, 1f, and 2b), but this was not a substorm but so called shock aurora with global brightening throughout the auroral oval without local breakup (Liou et al., 2003). The shock aurora was associated with a TEC enhancement from 7 to 11 TECU in the auroral oval (Figure 1g).

After 08:35 UT, the aurora became weaker and the auroral oval moved equatorward, with the latter being a typical substorm growth phase signature. The growth phase arc can be seen as a latitudinally thin arc starting at 8:38 UT at 65° MLAT in Figure 1e and at 66° MLAT Figure 1f, followed by equatorward motion. The equatorward motion of the growth phase arc was very rapid: The arc moved over 1.8°

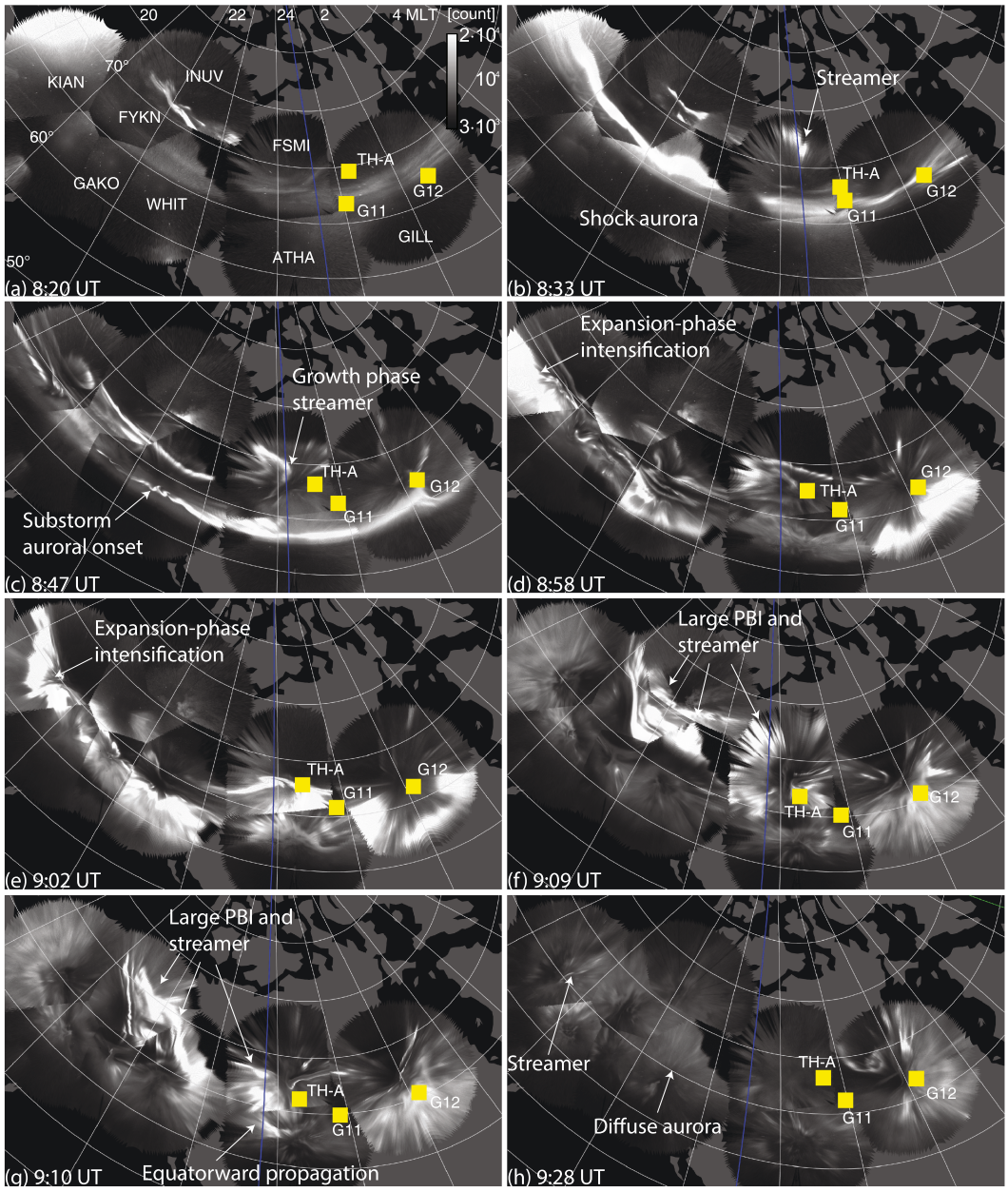

Figure 2. 2-D sequence of THEMIS ASI mosaics. The yellow dots show THEMIS-A, GOES-11, and GOES-12 satellite footprints using the T01 magnetic field model (Tsyganenko, 2002). The blue line marks magnetic midnight. The latitude and longitude contours are given every 5° and 15°.

MLAT in 10 min (or at a rate of 11° per hour), which is 2.2–5.5 times faster than that for typical substorms regardless of upstream conditions (2–5° per hour) (Coumans et al., 2007). The growth phase |*AL*| of 900 nT and 7 MA of upward/downward currents are also much larger than those for typical substorms: ~100 nT (Tanskanen, 2009) and ~0.2 MA (Anderson et al., 2018). The region of enhanced TEC also moved equatorward at the same rate.

The substorm auroral onset occurred at 63° MLAT along the equatorward-most arc at 08:46 UT (seen in Figure 2c). Movie S1 shows a small poleward expansion and surge at 08:47–08:50 UT in western Canada. The onset was followed by a series of brightenings along the poleward-expanding arc (Figures 1e, 1f, 2d, and 2e) and enhancements of |*AL*| (Figure 1c). |*AL*| reached 2,000 nT associated with the 09:02 UT auroral brightening (Figures 1f and 2e) and a large TEC enhancement reaching 38 TECU (a 20 TEC jump in

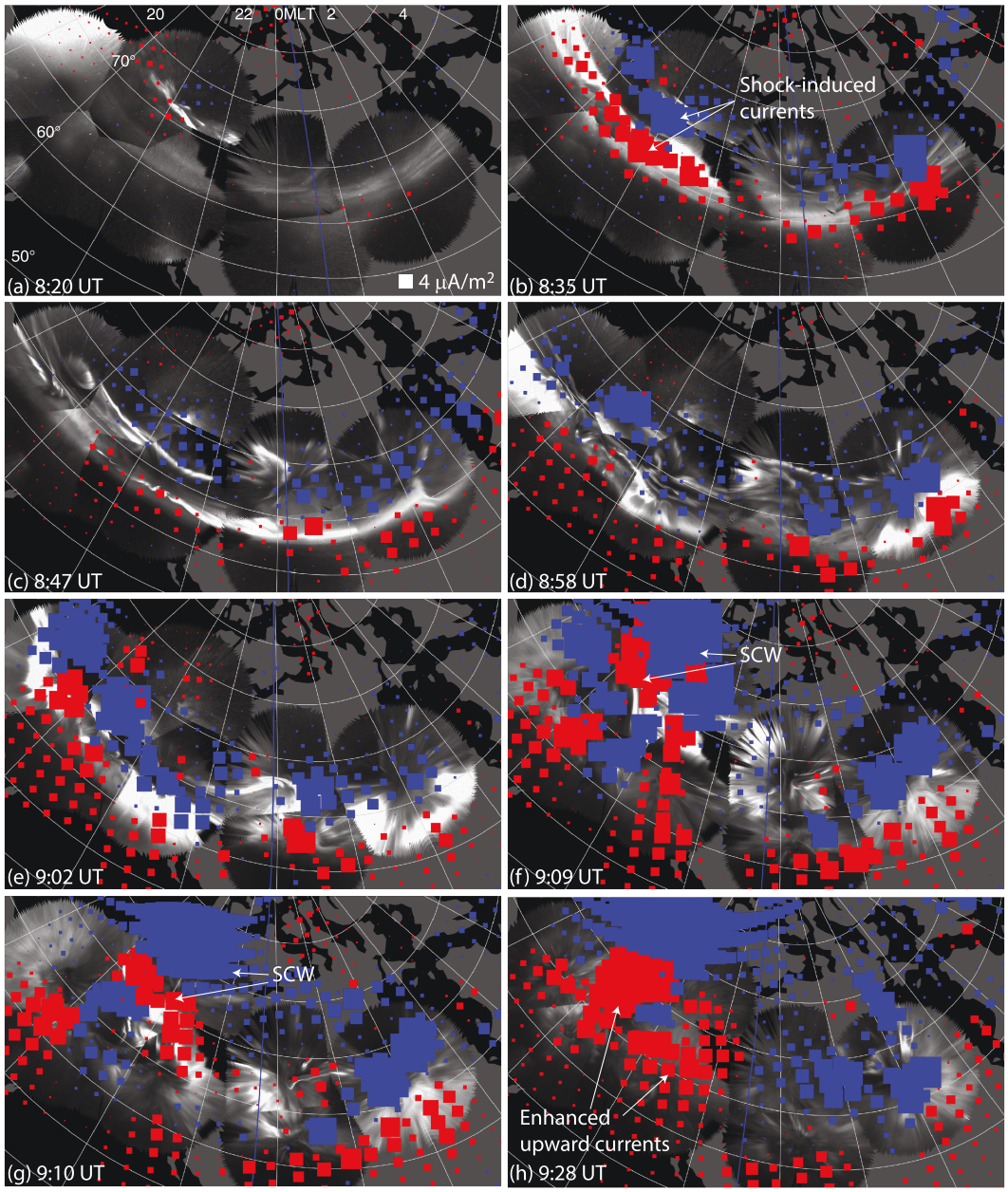

Figure 3. Upward (red) and downward (blue) currents overlaid onto the auroral images in Figure 2.

2 min, Figure 1g). The next brightening at 68° MLAT starting at 09:08 UT (seen in Figure 2f) was also intense, where |*AL*| increased to 2,300 nT and upward/downward currents became greater than 18 MA. This current is much larger than the nightside currents estimated by AMPERE (4 MA) for this event (Anderson et al., 2017). It is likely because the SECS currents from the ground magnetometers have higher temporal and longitudinal resolution, which resolves more localized and fast-varying currents. We checked that the SECS current density along the CHAMP satellite orbit in eastern Alaska at ~09:15 UT was comparable to the CHAMP magnetometer observation (not shown). The upward and downward currents were an order of magnitude larger than those for typical substorms (~1 MA (Anderson et al., 2018)). This brightening occurred along the poleward boundary of the auroral oval and was quickly accompanied with southeastward motion (Figures 1e and 2g). This led to an unusually large streamer, where the entire structure extends over 10° latitude (72–62° magnetic latitude [MLAT]) and 3.1 hr local time (21.4–0.5 magnetic local time [MLT]) with a southeastward tilt (cf. an

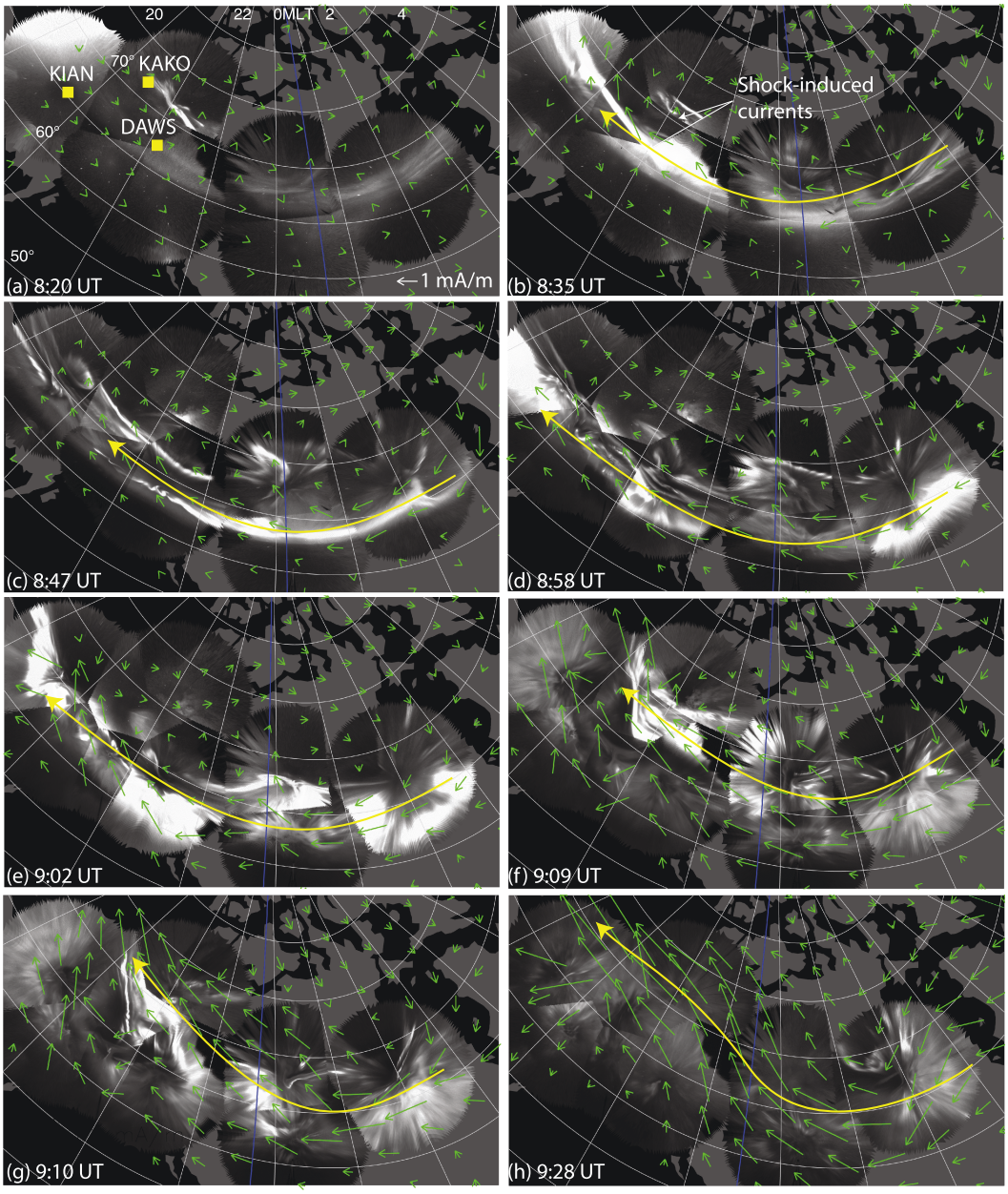

Figure 4. Horizontal currents overlaid onto the auroral images in Figure 2. Magnetometer stations at Kiana (KIAN), Dawson City (DAWS), and Kaktovik (KAKO) are indicated in panel (a). The location of most-intense currents are traced in yellow.

average streamer extends across 1.67 hr MLT; Gallardo-Lacourt et al., 2017). The large streamer contains smaller-scale streamers and seems to move as a group of streamers. TEC increased from 12 to 19 TECU 3 min. The eastern tip of the streamer reached the THEMIS-A satellite footprint. The streamer was long lasting (~10 min) and was followed by a few smaller streamers until ~09:30 UT (Figure 2h), which correspond to the peak |*AL*| of 2,700 nT. The peak THEMIS |*AL*| index was larger than that used by Connors et al. (2011) because of the addition of more stations after their work. Then the aurora and electrojet decayed under the northward IMF. The duration of the southward IMF was only about 1 hr, which could explain why the supersubstorm occurred under the small |*Dst*|. The southward IMF arrived after a quiet time, and the duration of the southward IMF was sufficiently long to drive the substorm but was too short to develop into a storm.

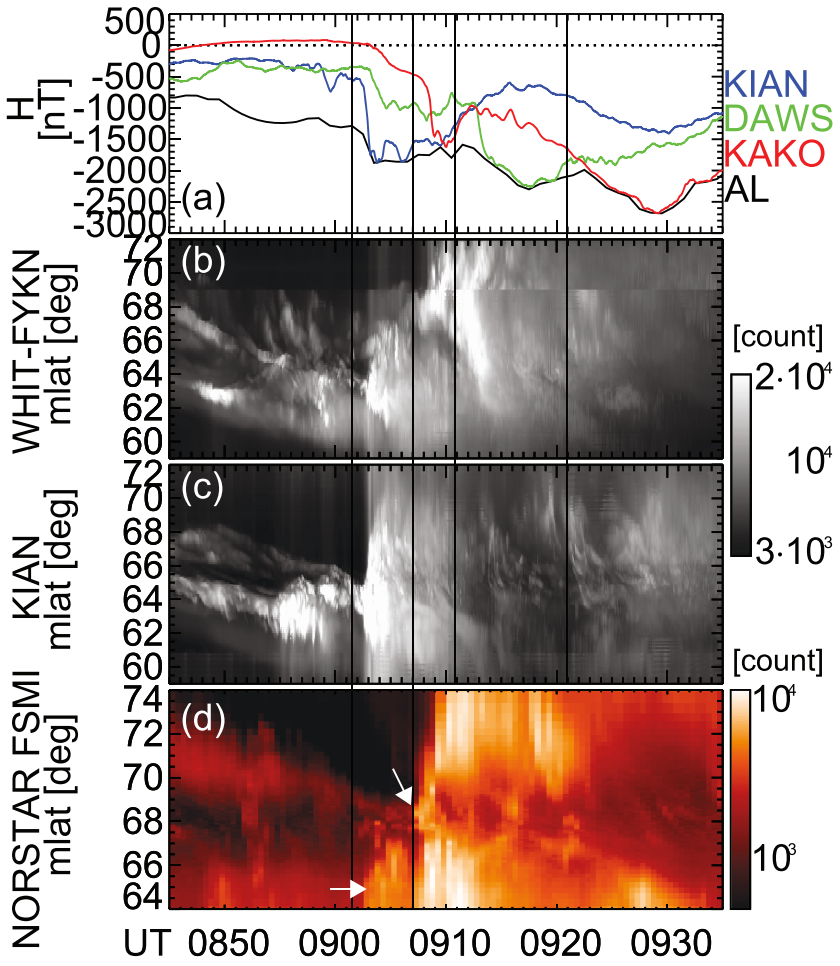

Figure 5. (a) THEMIS *AL* compared to the horizontal (*H*) magnetic field component at KIAN, DAWS, and KAKO. (b) THEMIS ASI keogram at WHIT and FYKN, (c) THEMIS ASI keogram at KIAN, and (d) NORSTAR FSMI ASI 630.0 nm keogram.

The sequence of |*AL*| enhancements started with the solar wind dynamic pressure enhancement. However, unlike the hypothesis that enhanced dynamic pressure triggers supersubstorms (Tsurutani et al., 2015), the pressure pulse in this event only caused the shock aurora and ~900 nT |*AL*| enhancement. The auroral onset occurred ~20 min after the shock, and the peak |*AL*| occurred 1 hr later under the period of steady dynamic pressure without an additional pressure pulse. The peak |*AL*| was established by a series of auroral and electrojet intensifications, and those intensifications do not correspond to the substorm onset but to activations that occurred during the substorm expansion phase. The extremely large PBI and streamer activation that occurred during the expansion phase ~20 min after the onset, and the weaker activations that occurred soon thereafter, were associated with the peak |*AL*| index. Considering the known relation between streamers and plasma sheet flows (Sergeev et al., 2004), this association indicates that localized and intense magnetotail reconnection and plasma sheet flows drove the large PBI, streamer, and the ionosphere currents producing the large |*AL*|. This is similar to what has been seen for classical substorms, during which the expansion phase streamers, and not the substorm onset, give rise to the maximum ground magnetic field depression (Engebretson et al., 2019; Lyons et al., 2013).

2.2. Spatial Evolution of the Ionospheric Currents

The upward, downward, and horizontal currents from the SECS method are overlaid onto the auroral images and shown in Figures 3 and 4. An east-west oriented sheet of upward currents was associated with the shock aurora in the pre-midnight sector (Figure 3b). Downward currents were located poleward of the

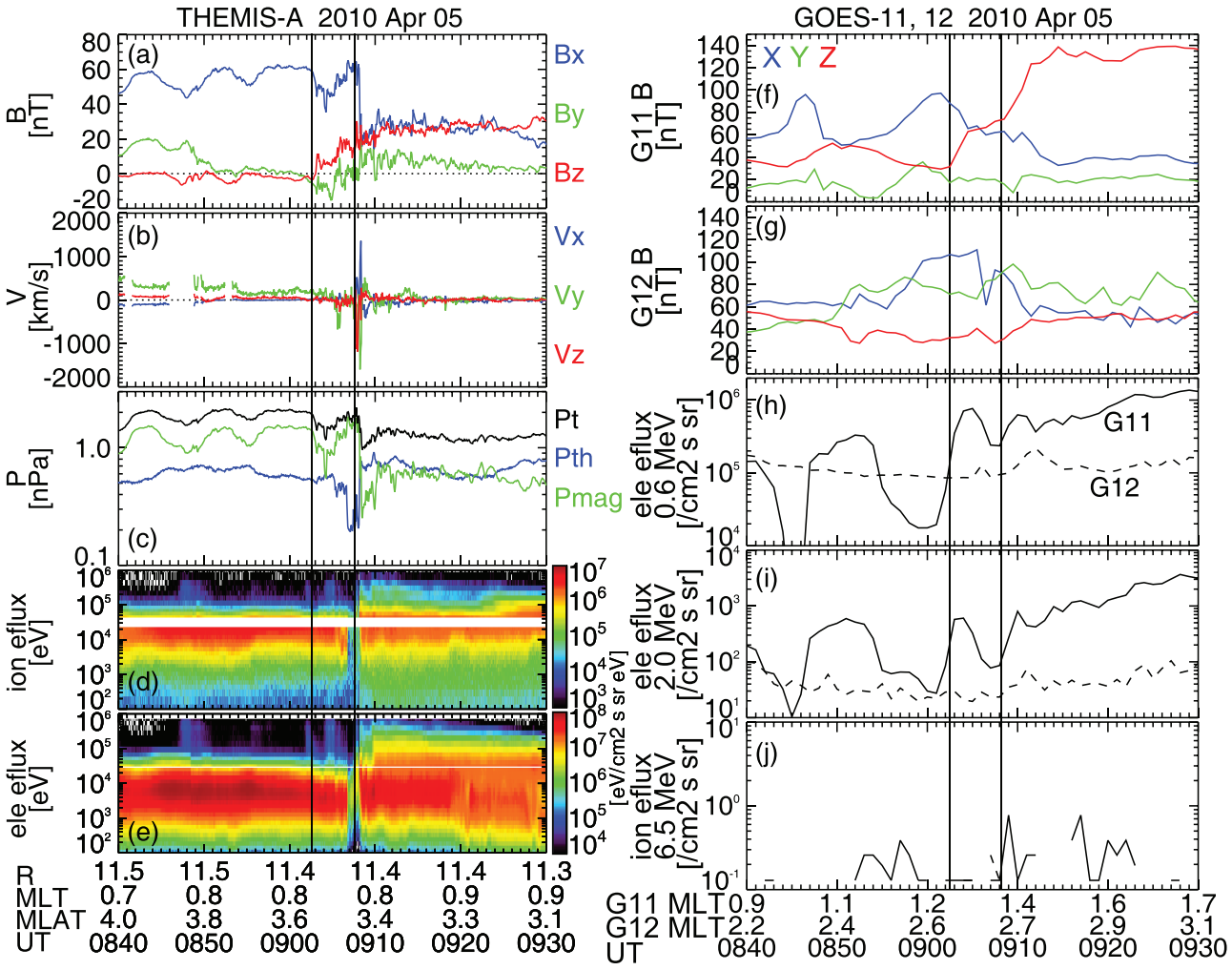

Figure 6. (ae) THEMIS-A measurements of the magnetic field, $E \times B$ drift velocity, pressure, and ion and electron energy flux. (f, g) Magnetic field from GOES-11 and GOES-12, (hk) fluxes of 0.6 MeV electrons, 2.0 MeV electrons, and 6.5 MeV ions. The two vertical lines mark two-step dipolarizations.

upward currents, and westward currents were located between the upward and downward currents (Figures 3b and 4b). Currents did not show clear changes during the auroral brightenings in the early expansion phase perhaps due to the limited spatial resolution (Figures 3c and 3d), but the brightening at 09:02 UT was detected as a localized intensification of upward and westward currents at 65° MLAT and 21 MLT (Figures 3e and 4e). The largest auroral brightening starting at 09:08 UT was associated with more intense and extended currents with the same orientation as the auroral streamer (seen in Figures 3f, 3g, 4f, and 4g). At those times, the tilted streamer marked the upward current portion of the substorm current wedge (SCW), and the downward currents were located to the east of it. The horizontal currents shifted poleward in accordance with the poleward-expanding aurora. Northwestward horizontal currents peaked between the upward and downward currents near the pre-midnight auroral poleward boundary, although the coarser spatial resolution of the horizontal currents does not adequately resolve spatial structure of the currents. Note that the peak upward and downward currents were only separated by ~1 hr MLT, despite that the enhanced auroral activity spread more broadly (beyond ±3 hr around midnight). The magnitude of the SCW was unusually high (10 $\mu A/m^2$) compared to that during typical substorms (a few $\mu A/m^2$; Hoffman et al., 1994). The currents then extended over a ~2 hr MLT width at the peak of $|AL|$ (Figure 3h). The azimuthally localized extent of the enhanced currents indicates that the current system that created the peak $|AL|$ is not a global-scale current system but is a localized SCW that abruptly intensified during the late expansion phase.

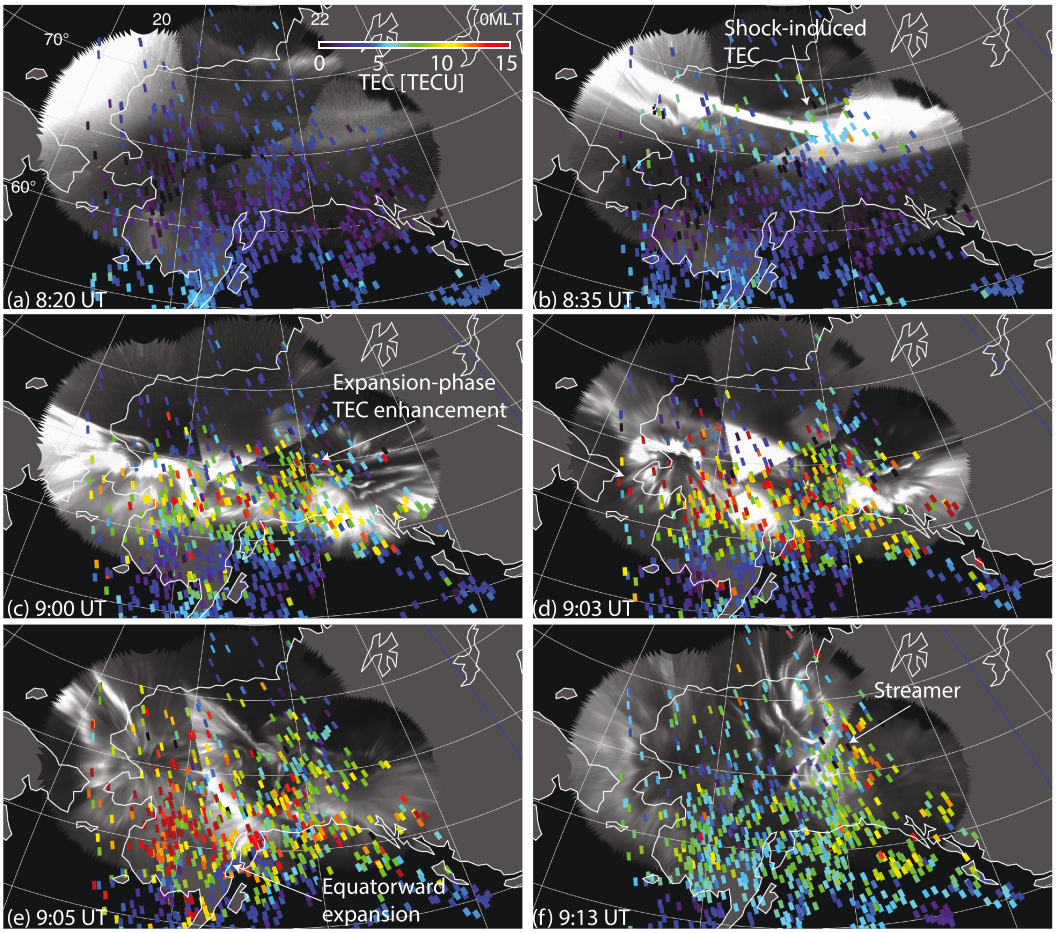

Figure 7. GPS TEC over Alaska overlaid onto the auroral images.

To show the location of the intense currents more precisely, we plotted magnetometer data from three representative stations in Figure 5a. Three successive enhancements in |*AL*| were detected by these three stations. The 1,700 nT |*AL*| deflection at 09:03 UT was seen at KIAN, where an auroral poleward expansion was detected (Figure 5c). KAKO detected the 09:08 UT PBI currents, and DAWS detected the currents associated with the equatorward-propagating streamer. The |*AL*| peak was seen at KAKO at 09:29 UT during the subsequent streamers. Because each magnetometer responded at different times, the intense currents were localized to the separation between the magnetometers or smaller (less than a few 100 km), and its current location dynamically changed over time.

The 630.0 nm meridian scanning photometer (MSP) data at Fort Smith (FSMI) are shown in Figure 5d. Auroral emission at this wavelength is more sensitive to low-energy precipitation than the white-light THEMIS ASI data and is useful to evaluate if auroral emission is located at the poleward boundary. It can be seen that the 09:02 UT auroral brightening started several degrees equatorward of the poleward-most auroral arc, while the 09:08 UT auroral brightening started along the poleward-most pre-existing arc (marked by the white arrows). Thus, the 09:02 UT brightening (and possibly earlier brightenings) was located within the auroral oval, while the 09:08 UT brightening is a PBI.

2.3. Nightside Magnetosphere

As shown in Figure 2g, the footprint of THEMIS-A was located near the large streamer. Although the magnetic field mapping during the disturbed time cannot give us precise mapping location, it is expected that the THEMIS-A footprint was in the vicinity of the streamer and that THEMIS-A therefore detected the

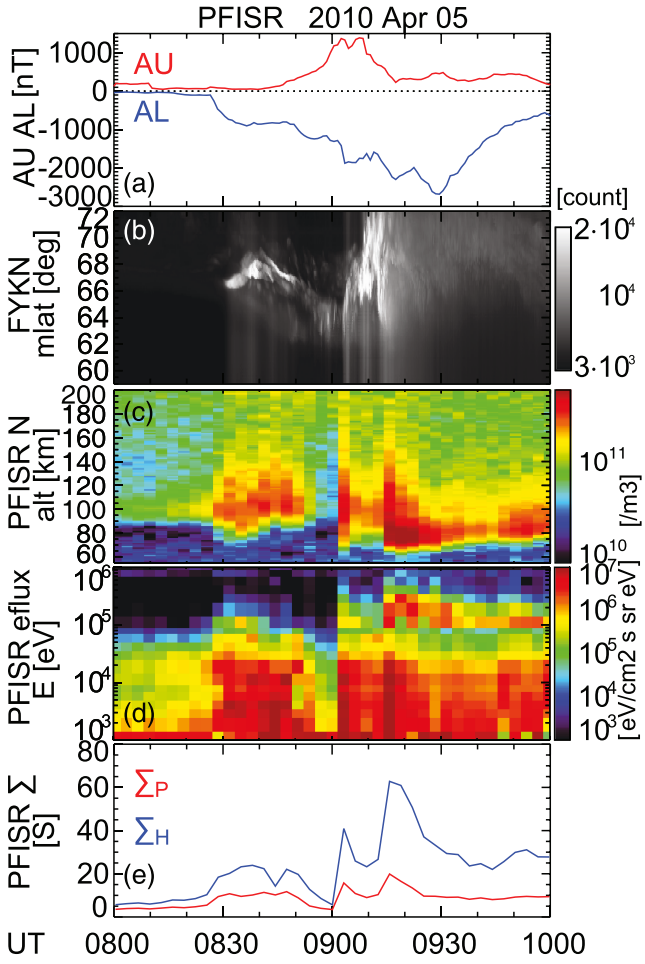

Figure 8. (a) THEMIS *AU* and *AL*, (b) THEMIS ASI keogram at FYKN, (c) PFISR plasma density, (d) precipitating energy flux, and (e) Hall and Pedersen conductances.

magnetospheric counterpart. The footprint of Geostationary Operational Environmental Satellite (GOES)-11, which detected the overdipolarization (Loto'aniu et al., 2015), was located near THEMIS-A.

THEMIS-A was located in the plasma sheet (β ~ 0.5, Figure 6c) except for a brief period (09:07–09:08 UT). THEMIS-A detected a two-step dipolarization at 09:03 and 09:08 UT, characterized by B_x reductions. Those two steps coincide well with two of the expansion-phase brightenings shown in Figures 1 and 5. The second step corresponds to the large PBI/streamer, and it was associated with the strong earthward $E \times B$ flow of 1,400 km/s. Particle acceleration was also extremely intense. Both ions and electrons show flux enhancements up to ~1 MeV despite being at 11.4 R_E radial distance. Considering again the connection between plasma sheet fast flows and auroral streamers (Sergeev et al., 2004), the large auroral streamer in this event corresponds to the unusually large dipolarization, injection, and fast flows in the plasma sheet.

THEMIS-A measured the total pressure reaching ~2 nPa during the growth phase, a few times larger than the total pressure during a typical substorm growth phase (Forsyth et al., 2014; Yue et al., 2015). The high pressure indicates a much larger amount of thermal energy accumulated in the plasma sheet.

The dipolarization at GOES-11 reached 140 nT in B_z (Figure 6f), exceeding the quiet-time level (~100 nT) and hence called overdipolarization (Connors et al., 2011; Loto'aniu et al., 2015). The dipolarization and relativistic electron fluxes (Figures 6h and 6i) at GOES-11 also had a two-step structure and occurred within 1 min from the time of the THEMIS-A measurements. The dipolarizations and electron flux enhancements were also detected at GOES-12 (1 MLT to the east of GOES-11) but were much smaller, indicating that GOES-12 observed the edge of an azimuthally localized dipolarization. Because injections have been associated with dipolarization (e.g., Gabrielse et al., 2014, 2016, 2017), the GOES observations suggest an azimuthally localized injection. The fact that the relativistic particle injections were observed is consistent with the finding by Dai et al. (2014, 2015) and Tang et al. (2016) for ~1,000 nT *AE* substorms, but the fluxes in the magnetotail and at geosynchronous orbit were 2 and 30 times larger in the present event, likely contributing to the anomaly of the Galaxy-15 satellite, which was located near GOES-11. An unusually large reconnection that released the large accumulation of energy could be the likely driver of the fast flow, overdipolarization, and particle acceleration.

2.4. Particle Precipitation and Neutral Wind

Here we examine the ionosphere density, conductance, plasma drift and neutral wind from GPS TEC, Poker Flat incoherent scatter radar (PFISR), and scanning Doppler imagers (SDIs) in Alaska around the supersubstorm location. Figure 7 presents 2-D distributions of the GPS TEC data. As in Figure 1g and section 2.1, TEC increased associated with the solar wind dynamic pressure enhancement, and the enhanced TEC was seen along the shock aurora (Figure 7b). TEC further increased during the expansion-phase auroral brightenings (Figure 7c) and reached the peak TEC (38 TECU) during one of the large brightenings (Figure 7d). The region of enhanced TEC extended poleward and equatorward as the aurora expanded poleward and equatorward (Figure 7e). The large auroral streamer was also associated with a localized TEC enhancement (Figure 7f).

The altitude profile of the plasma density along the magnetic field-aligned beam from PFISR is shown in Figure 8c. The PFISR density data were used to derive precipitating electron energy flux (Figure 8d), conductances (Figure 8e), and ion-neutral coupling time scale (Figure 9d) using methods described in our previous studies (Sivadas et al., 2017; Zou et al., 2018). Input parameters were obtained from

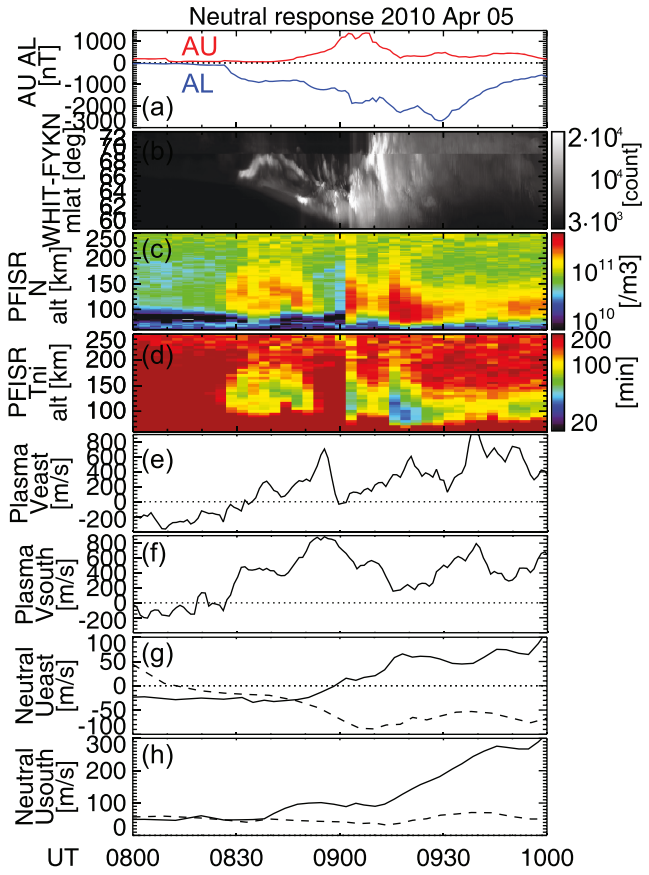

Figure 9. (a) THEMIS *AU and AL, (b) THEMIS* ASI keogram from WHIT and FYKN, (c) PFISR plasma density, (d) neutral-ion collision time scale, (e) eastward and (f) equatorward plasma drift averaged over 65°68° MLAT, and (g) eastward and (h) equatorward neutral wind averaged over 65°68° MLAT. The dashed lines in panels (g) and (h) show wind observations during a quiet day for a reference (3 April 2010).

PFISR (density, temperature, and ion composition), and the Mass Spectrometer Incoherent Scatter (MSIS), and International Reference Ionosphere (IRI) models. Collision frequencies of Schunk and Walker (1973) and Schunk and Nagy (1978) were used for the conductivity and ion-neutral time scale.

The interplanetary shock created enhanced density down to 70 km altitude at 08:35 UT. The inversion of the density data shows that this density enhancement was created by electron precipitation up to ~300 keV and a Hall conductance enhancement of 25 S. This was a more highly conducting portion of the ionosphere than for a typical substorm growth phase (a few S; Kirkwood et al., 1988).

The density increased again at 09:02 and 09:15 UT, corresponding to the expansion-phase auroral brightenings starting at 09:02 and 09:08 UT. Particularly noteworthy, the density enhancement after 09:15 UT was seen down to 60 km altitude, lower than that for the 1,400 nT |*AL*| event studied by Sivadas et al. (2017). The inferred precipitating energy flux in Figure 8d increased across all energies up to 1 MeV, by an order of magnitude or more. The energy distribution occasionally shows a peak at a few keV, which it could be due to a parallel potential drop over PFISR. At other times, the energy flux monotonically decreases with energy up to 100 keV, indicating that the parallel potential drop was less than 1 keV and precipitation is driven by magnetospheric particle acceleration and scattering. The flux peak at ~100 keV corresponds to the density peak at ~80–90 km altitude, indicating an additional acceleration process for particles of that energy. The fluxes are comparable to the measured level at THEMIS (Figure 6e, though an exact match is not expected due to the large local time separation between the radar and satellite). The ionosphere conductances also increased substantially (65 S Hall and 20 S Pedersen), which would allow for the intense electrojet of |*AL*| >2,500 nT. The conductance values, however, are comparable to typical substorms (Gjerloev & Hoffman, 2000; Kirkwood et al., 1988). Although 10 MeV protons could also reach ~60 km altitude, proton fluxes of those energies above 6.5 MeV at GOES were at a noise level (Figure 6j), and thus, the density enhancements at low altitudes were created by electron precipitation.

Figures 9e9h and 10 show plasma flow and neutral wind measurements. The plasma flow vectors were calculated by combining line-of-sight velocities from the PFISR beams looking at different directions (Heinselman & Nicolls, 2008). SDI measures F-region neutral wind and gives wind vectors using the technique described by Conde and Smith (1998). The flow and wind data were averaged over the PFISR coverage (65°68° MLAT). Soon before the interplanetary shock, the plasma flow was westward and the neutral wind was southwestward (Figure 10a). The westward flow is typical pre-midnight plasma convection, and the southwestward wind is also a typical wind due to the day-night pressure gradient and Coriolis force (Conde & Smith, 1998). The wind direction and strength right before the shock impact was nearly at the quiet-time wind level (dashed lines in Figures 9g and 9h). Because the neutral-ion coupling time scale was longer than a few hours (Figure 9d), the ion drag force was not effective at that time.

Soon after the shock arrival, the plasma flow switched to southeastward, aligned with the shock auroral arc (Figure 10b). The neutral wind did not immediately respond but started being deflected southeastward 10 min after the shock arrival (Figures 9g and 9h). This wind change deviates from the quiet-time wind and is thus in response to this specific event. The short response time of the neutral wind is likely due to enhanced ion drag as can be inferred from the shorter neutral-ion coupling time scale (Figure 9d). However, the wind speed remained low (~100 m/s) until the substorm onset (8:46 UT), and thus, the wind does not likely contribute to a precondition of the supersubstorm.

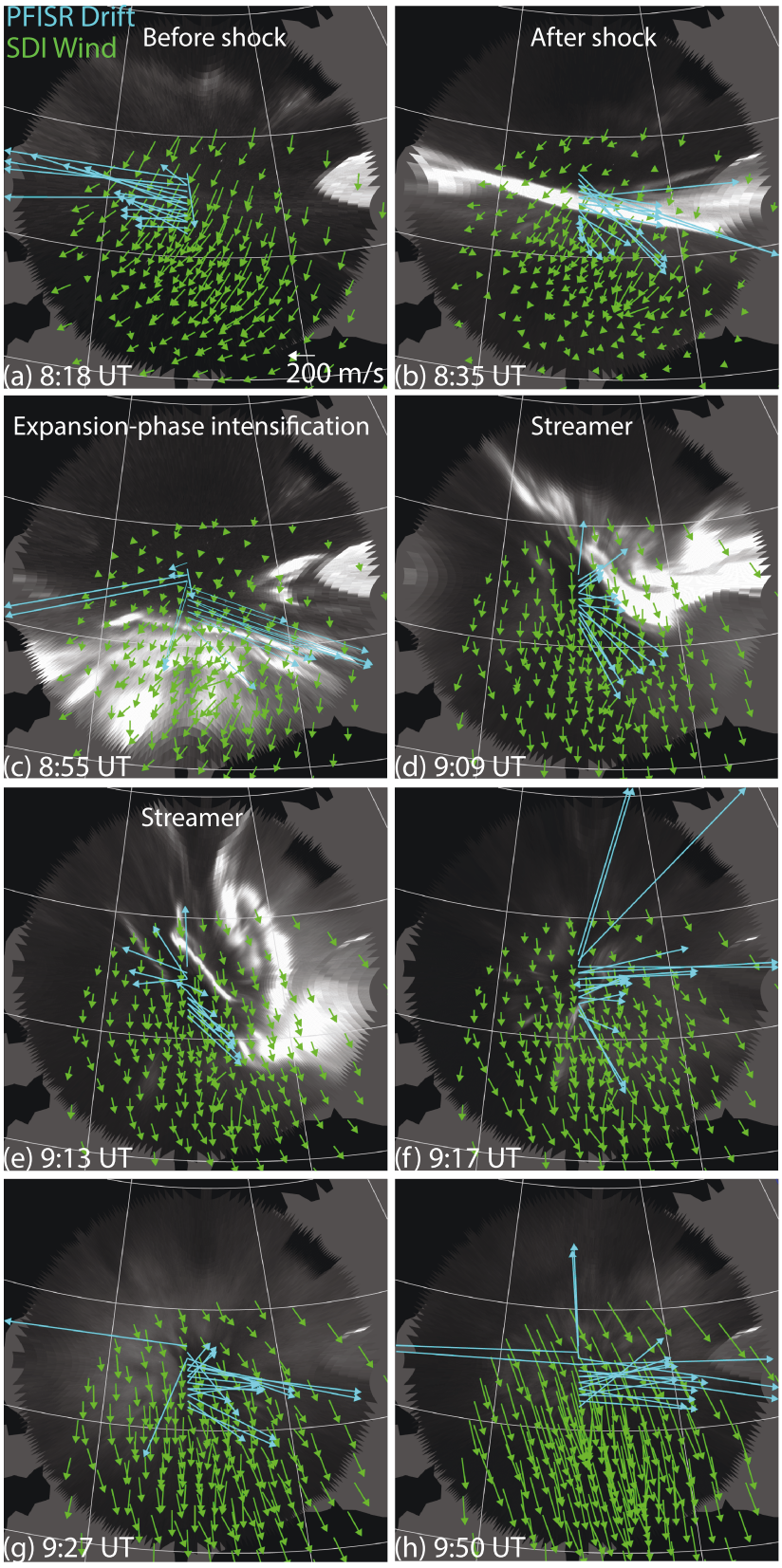

Figure 10. Plasma drift (cyan) and neutral wind (green) 2-D vectors overlaid on the FYKN THEMIS ASI.

After 09:02 UT, the plasma flow showed dynamic variations with a few enhancements and shears associated with the auroral intensifications (Figures 10c10g). The neutral wind rapidly increased more toward the direction of the plasma flow after 09:10 UT and peaked at 09:45 UT. This wind response is also likely due to the enhanced ion drag, and the ~35 min response time is consistent with the calculated neutral-ion coupling time scale (Figure 9d). The wind magnitude reached 280 m/s (250 m/s above the quiet-time background) at 09:45 UT. The wind speed is larger than the ~100 m/s change seen in typical substorms, although the response time scale is comparable to typical substorms (Anderson et al., 2011). The measured wind changes are driven by local forces because propagation of accelerated wind from outside the measurement area would take >1 hr to propagate across the field of view (~700 km) with the measured wind speed. Other forces such as pressure gradients could contribute to the wind variations. The Coriolis force is not effective because it would turn the southward wind to the west, but the measured wind turned from southwestward to southeastward. These results show unusually large ionospheric density and conductance, and fast neutral wind responses. Those are likely driven by the enhanced particle precipitation from the plasma sheet.

3. Conclusion

We presented M-I-T observations during the 5 April 2010 supersubstorm event and discussed driving processes and system responses. This event occurred during an elevated solar wind dynamic pressure and southward IMF B_z after an interplanetary shock, but unlike the shock-triggering hypothesis, the shock did not directly cause the supersubstorm. Instead, the shock created shock aurora and TEC enhancement followed by the unusually large growth phase of the substorm. The growth phase arc moved much more rapidly, and $|AL|$ and upward/downward currents increased much higher than those for typical substorms. The magnetotail total pressure, ionosphere density, precipitating electron fluxes, and conductances were also substantially elevated. The plasma drift and neutral wind in the pre-midnight auroral oval stayed at a typical level. The unusually rapid and large accumulation of energy in the magnetotail and the highly conducting ionosphere under the strong solar wind driving seem to have been the energy source of this supersubstorm.

The substorm auroral onset only showed a small brightening, and it was not directly connected to the largest auroral electrojet in this event. The expansion phase of the supersubstorm is composed of a series of auroral electrojet enhancements on the poleward-expanding auroral arc activity. One of them was associated with an extremely large PBI and streamer. Fast plasma sheet flows and intense particle injection, presumably driven by intense and localized magnetotail reconnection, have driven the large PBI and streamer. The supersubstorm electrojet is fed by a SCW associated with the PBI/streamer, and it was much more localized than the entire extent of the nightside auroral activity. The individual magnetometers also showed that the supersubstorm electrojets were localized to a few 100 km size and dynamically changed locations. The TEC structure was overall correlated well with the auroral structure and showed large enhancements associated with the auroral brightenings. The intense particle precipitation up to relativistic energies penetrated down to the D-region ionosphere and created unusually large conductance. The precipitation shortened the neutral-ion coupling time scale, and the neutral wind speed was larger than that for typical substorms. The ion drag is suggested to contribute to the wind acceleration.

These results emphasize the importance of magnetotail reconnection, plasma sheet flow channels, and particle acceleration processes for driving the extreme M-I-T responses. It is still, however, an open question why the reconnection was unusually intense and whether the measured M-I-T responses can be reproduced by simulation. Numerical modeling should be conducted to quantify the system responses. The observed responses documented in this study would be beneficial for the modeling community to test simulation capability of extreme events in the future.

Acknowledgments
This work was supported by NASA (Grants NNX17AL22G and 80NSSC18K0657) and NSF (Grants AGS-1907698, AGS-1762141), and AFOSR (Grant FA9559-16-1-0364). The THEMIS mission and all-sky imagers are supported by NASA (Contract NAS5-02099), CFI, and NSF (Grant AGS-1004736). The THEMIS, Geotail, TEC, PFISR, and SDI data were obtained online (through themis.ssl.berkeley.edu, cdaweb.gsfc.nasa.gov, http://cedar.openmadrigal.org, amisr.com, and sdi_server.gi.alaska.edu/sdiweb/index.asp). Data processing used SPEDAS V3.1 (Angelopoulos et al., 20192019). Data for the TEC processing are provided by many organizations including, in particular, UNAVCO, CDDIS, and National Geodetic Survey.

References

Anderson, B. J., Korth, H., Welling, D. T., Merkin, V. G., Wiltberger, M. J., Raeder, J., et al. (2017). Comparison of predictive estimates of high-latitude electrodynamics with observations of global-scale Birkeland currents. *Space Weather*, *15*, 352–373.

Anderson, B. J., Olson, C. N., Korth, H., Barnes, R. J., Waters, C. L., & Vines, S. K. (2018). Temporal and spatial development of global Birkeland currents. *Journal of Geophysical Research: Space Physics*, *123*, 4785–4808. https://doi.org/10.1029/2018JA025254

Anderson, C., Davies, T., Conde, M., Dyson, P., & Kosch, M. J. (2011). Spatial sampling of the thermospheric vertical wind field at auroral latitudes. *Journal of Geophysical Research*, *116*, A06320. https://doi.org/10.1029/2011JA016485

Angelopoulos, V., Cruce, P., Drozdov, A., Grimes, E. W., Hatzigeorgiu, N., King, D. A., et al. (2019). The Space Physics Environment Data Analysis System (SPEDAS). *Space Science Reviews*, *215*(1), 9. https://doi.org/10.1007/s11214-018-0576-4

Buzulukova, N., Fok, M.-C., Roelof, E., Redfern, J., Goldstein, J., Valek, P., & McComas, D. (2013). Comparative analysis of low-altitude ENA emissions in two substorms. *Journal of Geophysical Research: Space Physics*, *118*, 724–731. https://doi.org/10.1002/jgra.50103

Cander, L. (2016). Re-visit of ionosphere storm morphology with TEC datain the current solar cycle. *Journal of Atmospheric and Solar-Terrestrial Physics*, *138-139*, 187–205.

Clilverd, M. A., Rodger, C. J., Danskin, D., Usanova, M. E., Raita, T., Ulich, T., & Spanswick, E. L. (2012). Energetic particle injection, acceleration, and loss during the geomagnetic disturbances which upset Galaxy 15. *Journal of Geophysical Research*, *117*, A12213. https://doi.org/10.1029/2012JA018175

Conde, M., & Smith, R. W. (1998). Spatial structure in the thermospheric horizontal wind above Poker Flat, Alaska, during solar minimum. *Journal of Geophysical Research*, *103*(A5), 9449–9471. https://doi.org/10.1029/97JA03331

Connors, M., Russell, C. T., & Angelopoulos, V. (2011). Magnetic flux transfer in the 5 April 2010 Galaxy 15 substorm: An unprecedented observation. *Annales de Geophysique*, *29*, 619–622.

Coumans, V., Blockx, C., Gérard, J.-C., Hubert, B., & Connors, M. (2007). Global morphology of substorm growth phases observed by the IMAGE-SI12 imager. *Journal of Geophysical Research*, *112*, A11211. https://doi.org/10.1029/2007JA012329

Dai, L., Wang, C., Duan, S., He, Z., Wygant, J. R., Cattell, C. A., et al. (2015). Near-Earth injection of MeV electrons associated with intense dipolarization electric fields: Van Allen Probes observations. *Geophysical Research Letters*, *42*, 6170–6179. https://doi.org/10.1002/2015GL064955

Dai, L., Wygant, J. R., Cattell, C. A., Thaller, S., Kersten, K., Breneman, A., et al. (2014). Evidence for injection of relativistic electrons into the Earth's outer radiation belt via intense substorm electric fields. *Geophysical Research Letters*, *41*, 1133–1141. https://doi.org/10.1002/2014GL059228

Engebretson, M. J., Steinmetz, E. S., Posch, J. L., Pilipenko, V. A., Moldwin, M. B., Connors, M. G., et al. (2019). Nighttime magnetic perturbation events observed in Arctic Canada: 2. Multiple-instrument observations. *Journal of Geophysical Research: Space Physics*, *124*, 7459–7476. https://doi.org/10.1029/2019JA026797

Forsyth, C., Watt, C. E., Rae, I. J., Fazakerley, A. N., Kalmoni, N. M., Freeman, M. P., et al. (2014). Increases in plasma sheet temperature with solar wind driving during substorm growth phases. *Geophysical Research Letters*, *41*, 8713–8721. https://doi.org/10.1002/2014GL062400

Gabrielse, C., Angelopoulos, V., Harris, C., Artemyev, A., Kepko, L., & Runov, A. (2017). Extensive electron transport and energization via multiple, localized dipolarizing flux bundles. *Journal of Geophysical Research: Space Physics*, *122*, 5059–5076. https://doi.org/10.1002/2017JA023981

Gabrielse, C., Angelopoulos, V., Runov, A., & Turner, D. L. (2014). Statistical characteristics of particle injections throughout the equatorial magnetotail. *Journal of Geophysical Research: Space Physics*, *119*, 2512–2535. https://doi.org/10.1002/2013JA019638

Gabrielse, C., Harris, C., Angelopoulos, V., Artemyev, A., & Runov, A. (2016). The role of localized inductive electric fields in electron injections around dipolarizing flux bundles. *Journal of Geophysical Research: Space Physics*, *121*, 9560–9585. https://doi.org/10.1002/2016JA023061

Gallardo-Lacourt, B., Nishimura, Y., Lyons, L. R., Mishin, E. V., Ruohoniemi, J. M., Donovan, E. F., et al. (2017). Influence of auroral streamers on rapid evolution of ionospheric SAPS flows. *Journal of Geophysical Research: Space Physics*, *122*, 12,406–12,420. https://doi.org/10.1002/2017JA024198

Gjerloev, J. W., & Hoffman, R. A. (2000). Height-integrated conductivity in auroral substorms. 2. Modelling. *Journal of Geophysical Research*, *105*, 227.

Hajra, R., Tsurutani, B. T., Echer, E., Gonzalez, W. D., & Gjerloev, J. W. (2016). Supersubstorms (SML < −2500 nT): Magnetic storm and solar cycle dependences. *Journal of Geophysical Research: Space Physics*, *121*, 7805–7816. https://doi.org/10.1002/2015JA021835

Heinselman, C. J., & Nicolls, M. J. (2008). A Bayesian approach to electric field and E-region neutral wind estimation with the Poker Flat advanced modular incoherent scatter radar. *Radio Science*, *43*, RS5013. https://doi.org/10.1029/2007RS003805

Hoffman, R. A., Fujii, R., & Sugiura, M. (1994). Characteristics of the field-aligned current system in the nighttime sector during auroral substorms. *Journal of Geophysical Research*, *99*(A11), 21,303–21,325. https://doi.org/10.1029/94JA01659

Keesee, A. M., Chen, M. W., Scime, E. E., & Lui, A. T. Y. (2014). Regions of ion energization observed during the Galaxy-15 substorm with TWINS. *Journal of Geophysical Research: Space Physics*, *119*, 8274–8287. https://doi.org/10.1002/2014JA020466

Kinrade, J., Mitchell, C. N., Yin, P., Smith, N., Jarvis, M. J., Maxfield, D. J., et al. (2012). Ionospheric scintillation over Antarctica during the storm of 5–6 April 2010. *Journal of Geophysical Research*, *117*, A05304. https://doi.org/10.1029/2011JA017073

Kirkwood, S., Opgenoorth, H., & Murphree, J. S. (1988). Ionospheric conductivities, electric fields and currents associated with auroral substorms measured by the EISCAT radar. *Planetary and Space Science*, *36*(12), 1359–1380. https://doi.org/10.1016/0032-0633(88)90005-0

Koons, H., & Fennell, J. (2006). Space weather effects on communications satellites. *Radio Science Bulletin No*, *316*, 27.

Liou, K., Newell, P. T., Meng, C.-I., Wu, C.-C., & Lepping, R. P. (2003). Investigation of external triggering of substorms with Polar ultraviolet imager observations. *Journal of Geophysical Research*, *108*(A10), 1364. https://doi.org/10.1029/2003JA009984

Liu, Y., Luhmann, J. G., Bale, S. D., & Lin, R. P. (2011). Solar source and heliospheric consequences of the 2010 April 3 coronal mass ejection: A comprehensive view. *The Astrophysical Journal*, *734*, 84. https://doi.org/10.1088/0004-637X

Loto'aniu, T. M., Singer, H. J., Rodriguez, J. V., Green, J., Denig, W., Biesecker, D., & Angelopoulos, V. (2015). Space weather conditions during the Galaxy 15 spacecraft anomaly. *Space Weather*, *13*, 484–502. https://doi.org/10.1002/2015SW001239

Lu, G., Hagan, M. E., Häusler, K., Doornbos, E., Bruinsma, S., Anderson, B. J., & Korth, H. (2014). Global ionospheric and thermospheric response to the 5 April 2010 geomagnetic storm: An integrated data-model investigation. *Journal of Geophysical Research: Space Physics*, *119*, 10,358–10,375. https://doi.org/10.1002/2014JA020555

Lyons, L. R., Nishimura, Y., Donovan, E., & Angelopoulos, V. (2013). Distinction between auroral substorm onset and traditional ground magnetic onset signatures. *Journal of Geophysical Research: Space Physics*, *118*, 4080–4092. https://doi.org/10.1002/jgra.50384

Prikryl, P., Spogli, L., Jayachandran, P. T., Kinrade, J., Mitchell, C. N., Ning, B., et al. (2011). Interhemispheric comparison of GPS phase scintillation at high latitudes during the magnetic-cloud-induced geomagnetic storm of 5–7 April 2010. *Annals of Geophysics-Germany*, *29*(12), 2287–2304. https://doi.org/10.5194/angeo-29-2287-2011

Schunk, R. W., & Nagy, A. F. (1978). Electron temperatures in the F region of the ionosphere: Theory and observations. *Reviews of Geophysics*, *16*(3), 355–399. https://doi.org/10.1029/RG016i003p00355

Schunk, R. W., & Walker, J. C. G. (1973). Theoretical ion densities in the lower ionosphere. *Planetary and Space Science*, *21*(11), 1875–1896. https://doi.org/10.1016/0032-0633(73)90118-9

Sergeev, V. A., Liou, K., Newell, P. T., Ohtani, S.-I., Hairston, M. R., & Rich, F. (2004). Auroral streamers: Characteristics of associated precipitation, convection and field-aligned currents. *Annales Geophysicae*, *22*(2), 537–548. https://doi.org/10.5194/angeo-22-537-2004

Sivadas, N., Semeter, J., Nishimura, Y., & Kero, A. (2017). Simultaneous measurements of substorm-related electron energization in the ionosphere and the plasma sheet. *Journal of Geophysical Research: Space Physics*, *122*, 10,528–10,547. https://doi.org/10.1002/2017JA023995

Tang, C. L., Zhang, J.-C., Reeves, G. D., Su, Z. P., Baker, D. N., Spence, H. E., et al. (2016). Prompt enhancement of the Earth's outer radiation belt due to substorm electron injections. *Journal of Geophysical Research: Space Physics*, *121*, 11,826–11,838. https://doi.org/10.1002/2016JA023550

Tanskanen, E. I. (2009). A comprehensive high-throughput analysis of substorms observed by IMAGE magnetometer network: Years 1993–2003 examined. *Journal of Geophysical Research*, *114*, A05204. https://doi.org/10.1029/2008JA013682

Tsurutani, B. T., Hajra, R., Echer, E., & Gjerloev, J. W. (2015). Extremely intense (SML < −2500 nT) substorms: Isolated events that are externally triggered? *Annales Geophysicae*, *33*, 519–524.

Tsyganenko, N. A. (2002). A model of the near magnetosphere with a dawn-dusk asymmetry: 1. Mathematical structure. *Journal of Geophysical Research*, *107*(A8), 1179. https://doi.org/10.1029/2001JA000219

Victor, N. J., Manu, S., Frank-Kamenetsky, A. V., Panneerselvam, C., Anil Kumar, C. P., & Elango, P. (2016). Network of observations on the atmospheric electrical parameters during geomagnetic storm on 5 April 2010. *Journal of Geophysical Research: Space Physics*, *121*, 2407–2417. https://doi.org/10.1002/2015JA022080

Vierinen, J., Coster, A. J., Rideout, W. C., Erickson, P. J., & Norberg, J. (2016). Statistical framework for estimating GNSS bias. *Atmospheric Measurement Techniques*, *9*, 1303–1312. https://doi.org/10.5194/amt-9-1303-2016

Weygand, J. M., Amm, O., Viljanen, A., Angelopoulos, V., Murr, D., Engebretson, M. J., et al. (2011). Application and validation of the spherical elementary currents systems technique for deriving ionospheric equivalent currents with the North American and Greenland ground magnetometer arrays. *Journal of Geophysical Research*, *116*, A03305. https://doi.org/10.1029/2010JA016177

Yue, C., Nishimura, Y., Lyons, L. R., Angelopoulos, V., Donovan, E. F., Shi, Q., et al. (2013). Coordinated THEMIS spacecraft and all-sky imager observations of interplanetary shock effects on plasma sheet flow bursts, poleward boundary intensifications, and streamers. *Journal of Geophysical Research: Space Physics*, *118*, 3346–3356. https://doi.org/10.1002/jgra.50372

Yue, C., Wang, C., Lyons, L., Wang, Y., Hsu, T., Henderson, M., et al. (2015). A 2-D empirical plasma sheet pressure model for substorm growth phase using the support vector regression machine. *Journal of Geophysical Research: Space Physics*, *120*, 1957–1973. https://doi.org/10.1002/2014JA020787

Zou, Y., Nishimura, Y., Lyons, L., Conde, M., Varney, R., Angelopoulos, V., & Mende, S. (2018). Mesoscale F region neutral winds associated with quasi-steady and transient nightside auroral forms. *Journal of Geophysical Research: Space Physics*, *123*, 7968–7984. https://doi.org/10.1029/2018JA025457